Design and Analysis of Upwind-Biased Discontinuous Galerkin Methods with Optimal Dispersion Properties

Xiaopei Cheng [1], Fengna Yan [2], Yan Jiang [3 4], Ziqiang Cheng [5]

Abstract

In this paper, we systematically investigate the dispersion properties of discontinuous Galerkin (DG) methods with upwind-biased numerical fluxes. By introducing four evaluation criteria based on the integrated error between the exact and numerical dispersion relations in different integration intervals or the maximum resolvable wavenumber, we obtain optimal values of the flux parameter for the DG method employing polynomials ranging from first-degree to fifth-degree. These optimal schemes are applied to a series of numerical examples, including a linear scalar equation, a system of linear equations, a spherical wave, and nozzle flow. Numerical results demonstrate that the optimal DG schemes produce smaller numerical errors than the standard DG schemes with upwind fluxes for scalar problems and with Lax–Friedrichs fluxes for system problems.

Keywords discontinuous Galerkin method; dispersion analysis; upwind-biased flux; computational aeroacoustics

1 Introduction

Dispersion analysis [4, 5, 10, 8, 17, 27] is a frequency-domain approach for assessing how accurately a numerical scheme propagates waves, with particular emphasis on its numerical dispersion relation. For a physical wave, the dispersion relation links frequency and wavenumber and therefore determines important dispersive properties such as phase velocity and group velocity. This issue is especially critical in computational aeroacoustics (CAA) [9, 11], where low amplitude acoustic waves must be transported over long

[1]The School of Mathematics, Hefei University of Technology, Hefei, Anhui 230009, China. Email: cxp0221@mail.hfut.edu.cn.

[2]The School of Mathematics, Hefei University of Technology, Hefei, Anhui, 230009, China. E-mail: fnyan@hfut.edu.cn.

[3]School of Mathematical Sciences, University of Science and Technology of China, Hefei, Anhui 230026, China. E-mail: jiangy@ustc.edu.cn.

[4]Laoshan Laboratory, Qingdao 266237, China.

[5]The School of Mathematics, Hefei University of Technology, Hefei, Anhui 230009, China. Email: czq10491@hfut.edu.cn.

distances with minimal phase error and numerical dissipation. To improve the accuracy of long-range wave propagation, dispersion-relation-preserving (DRP) schemes are designed to match the target dispersion relation over a prescribed band of wavenumbers[5, 30, 31]. Subsequently, considerable attention has been devoted to the development of DRP schemes. For example, an optimized upwind DRP finite-difference scheme is developed [10] to improve short-wavelength resolution without introducing explicit artificial damping, and the grid-optimized DRP (GODRP) framework [20] extended this traditional DRP finite-difference schemes to nonuniform Cartesian and curvilinear grids by locally optimizing stencil coefficients. More recently, [8] introduced a scale-aware DRP scheme that adaptively adjusts dispersion and dissipation using a scale sensor, thereby maintaining accuracy over a wide range of wavenumbers. However, most of the above developments have been carried out within the finite-difference framework. Beyond this setting, an analysis revealed that the discontinuous Galerkin (DG) scheme possesses excellent dispersion properties comparable to the DRP scheme, making it a very promising numerical method in CAA [1].

The DG method has gained widespread attention, owing to a range of attractive properties, including high parallel efficiency, high-order accuracy, compactness, favorable wave propagation properties, *hp* adaptivity and suitability for handling complex boundaries. It was originally introduced by Reed and Hill for solving the neutron transport equation [15], and was later developed into a powerful framework for hyperbolic conservation laws by Cockburn and Shu [16, 12, 13, 14], eventually becoming an important class of numerical methods in computational fluid dynamics. The dispersive behavior of DG methods has been the subject of numerous investigations. Ainsworth [17] analyzed the dispersion and dissipation properties of high-order *hp*-DG discretizations and established error decay rates in several limits. For linear advection equation, Sherwin [21] studied semi-discrete dispersion relations for both continuous and discontinuous Galerkin formulations, showing that while their dispersion behavior is comparable, the DG formulation is inherently more dissipative. Hu et al. [22] performed a systematic analysis of dispersion and dissipation properties for DG methods applied to wave propagation problems, including both one-dimensional advection and two-dimensional wave equations. Liu et al. [23] proposed nonuniform time-stepping Runge–Kutta discontinuous Galerkin (RKDG) methods with interface coupling to maintain low dispersion and dissipation in CAA simulations. Recently, Yu et al. [32] studied the dispersion and dissipation of two fully discrete schemes for linear convection based on the global spectral analysis (GSA) [18, 6, 7]. However, most existing dispersion studies of DG methods are conducted under the standard upwind numerical flux, which limits

the flexibility to obtain potentially more optimal schemes. This motivates the development of more flexible flux formulations that can better balance stability and wave resolution, and yield improved dispersion and dissipation characteristics over a wider range of wavenumbers.

In this work, we focus on the upwind-biased numerical flux, which contains a tunable parameter that introduces additional degrees of freedom for DG method. This flux was introduced in [2], where its stability and optimal error estimates were derived for DG discretizations of linear hyperbolic problems in one and multiple dimensions. After that, many related studies were developed. For instance, Meng et al. [26] investigated DG methods with upwind-biased fluxes for one-dimensional linear hyperbolic equations with degenerate variable coefficients, proving L^2 stability, well-posedness, and optimal a priori error estimates, while these results were extended to the two-dimensional case in [25]. The impact of upwind-biased fluxes on superconvergence was analyzed in [3], showing that the error constants were governed by the interplay between flux selection and polynomial degree. And Xu et al. [24] provided local error estimates for RKDG methods with upwind-biased fluxes for one-dimensional linear hyperbolic equations with discontinuous initial data.

While most existing studies concentrate on stability properties or error estimates, this paper adopts a dispersion analysis perspective, aiming to aim is to identify parameter choices that provide optimal numerical dispersion relations. In the semi-discrete DG formulation, the upwind-biased numerical fluxes introduces an additional parameter, increasing the complexity of the dispersion analysis compared with the standard upwind flux. However, this additional parameter introduces extra freedom that holds the potential for reducing dispersion errors. Therefore, a linear scalar problem is analyzed to derive the parameter expression that yields the optimal dispersion relation. Moreover, this optimal dispersion properties can be systematically extended to one-dimensional linear systems, demonstrating the applicability of the proposed dispersion optimization framework beyond scalar equations. The resulting schemes are further applied to a series of wave propagation problems, which are classical and challenging benchmarks in computational aeroacoustics and the numerical results demonstrate excellent performance.

The remainder of this paper is organized as follows. In Sec. 2, we introduce the DG formulation with upwind-biased numerical fluxes. Dispersion analysis is performed in Sec. 3 to identify flux parameters that yield optimal dispersion properties. Sec. 4 extends the results to one-dimensional linear systems. Numerical experiments are presented in Sec. 5 to validate the analysis, and concluding remarks are given in Sec. 6.

2 DG Methods with Upwind-Biased Nmerical Flux

In this section, we introduce the DG method with upwind-biased fluxes. Consider the following linear advection equation:

$$u_t + u_x = 0, \quad a \le x \le b, \ t > 0. \tag{2.1}$$

Assume that the computational domain is covered by a uniform grid, consisting of cells $I_j = \left[x_{j-\frac{1}{2}}, x_{j+\frac{1}{2}}\right]$ for $1 \le j \le N$, where

$$a = x_{\frac{1}{2}} < x_{\frac{3}{2}} < \cdots < x_{N+\frac{1}{2}} = b.$$

We denote the mesh size by $h = x_{j+\frac{1}{2}} - x_{j-\frac{1}{2}}$ and the midpoint of each cell by $x_j = \frac{1}{2}\left(x_{j+\frac{1}{2}} + x_{j-\frac{1}{2}}\right)$. We define the finite element space of piecewise polynomials as

$$V_h^q = \left\{v \ : \ v\,|_{I_j} \in P^q\left(I_j\right); \ j = 1, 2, \cdots, N\right\}, \tag{2.2}$$

where $P^q(I_j)$ denotes the space of polynomials of degree at most q. For any $v \in V_h^q$, we denote $v_{j+\frac{1}{2}}^-$ and $v_{j+\frac{1}{2}}^+$ the left limit and right limit of the function v at the cell interface $x_{j+\frac{1}{2}}$, respectively. In this work, the Legendre polynomials are employed as local basis functions.

The semi-discrete DG method for solving (2.1) is given as follows: find the unique $u_h = u_h(t) \in V_h^q$ such that for all test functions $v \in V_h^q$ and all $1 \le j \le N$,

$$\int_{I_j} (u_h)_t \, v dx = \int_{I_j} u_h v_x dx - \left(\hat{u}_{j+\frac{1}{2}} v_{j+\frac{1}{2}}^- - \hat{u}_{j-\frac{1}{2}} v_{j-\frac{1}{2}}^+\right). \tag{2.3}$$

Here $\hat{u}_{j+\frac{1}{2}} = \hat{u}(u_{j+\frac{1}{2}}^-, u_{j+\frac{1}{2}}^+)$ denotes the numerical flux at the interface $x_{j+\frac{1}{2}}$, which satisfies the conditions of consistency, continuity and monotonicity [34]. In this paper, we employ the upwind-biased flux

$$\hat{u}(u^-, u^+) = \theta u^- + (1-\theta)\, u^+, \ \ \theta > \frac{1}{2}. \tag{2.4}$$

Here, the parameter $\theta > \frac{1}{2}$ is taken following the L^2 stability analysis given in [2] and for linear advection, it ensures non-negative dissipation. Note that (2.4) is not monotone when $\theta \in (\frac{1}{2}, 1)$. But this does not affect the stability and convergence of the numerical solution. The third-order TVD Runge-Kutta method [33] is employed for time discretization.

In this paper, we restrict our attention to the cases from $q = 1$ to 5. The corresponding schemes achieve $(q+1)$-th order accuracy in space and third-order accuracy in time. These schemes are denoted by DG-P^q for each q.

3 Optimal Dispersive Property Parameters

In order to obtain the optimal numerical dispersion relation, an optimal value of θ must be selected for each scheme. Following [2], we restrict our attention to $\theta > \frac{1}{2}$ and perform the parameter search over $(\frac{1}{2}, 2]$. This interval contains the standard upwind flux ($\theta = 1$) and, since the numerical dissipation increases with θ according to [2], taking $\theta \leq 2$ provides a practical upper bound that avoids overly dissipative schemes while still offering sufficient flexibility to tune the dispersion–dissipation balance.

Since the admissible set contains infinitely many values of θ, additional criteria are required to select the parameter that yields favorable dispersion behavior. Following Tam's DRP philosophy [5], we measure dispersion accuracy using an integrated error over a prescribed wavenumber range

$$E(K_c) = \int_0^{K_c} \left|\omega h - \mathrm{Re}(\tilde{\omega} h)\right| d(kh), \tag{3.1}$$

where K_c denotes the cutoff wavenumber that defines the target band in Fourier space. Here k denotes the physical wavenumber and ω is the corresponding physical angular frequency. For the linear advection equation with unit wave speed, the exact dispersion relation reduces to $\omega = k$, and therefore $\omega h = kh$, which represents the dimensionless wavenumber. $\tilde{\omega} h$ denotes the numerical dimensionless wavenumber and will be computed below.

3.1 The Dispersion and Dissipation Realtions of Semi-Discrete Case

Following the analysis in [1], we consider the linear advection equation whose initial condition is given by a single Fourier wave:

$$\begin{cases} u_t + u_x = 0, \\ u\left(x, 0\right) = e^{ikx}, \end{cases} \tag{3.2}$$

whose exact solution is

$$u\left(x, t\right) = e^{i(kx - \omega t)}, \ \ \omega = k. \tag{3.3}$$

Let P_h denote the L^2-projection operator onto the finite element space V_h^q, which provides the numerical initial condition for the DG scheme. Applying the projection to the initial data yields

$$u_h\left(x, 0\right) = P_h\left(e^{ikx}\right), \tag{3.4}$$

where $P_h\left(e^{ikx}\right)$ satisfies:

$$\int_{I_j}\left(P_h\left(e^{ikx}\right)-e^{ikx}\right)vdx=0,\ \forall v\in V_h^q,\ j=1,2,\cdots,N. \tag{3.5}$$

The numerical solution on each cell I_j can be expressed as

$$u_h\left(x,t\right)|_{I_j}=\sum_{m=0}^{q}u_m^j\left(t\right)\varphi_m^j\left(x\right), \tag{3.6}$$

where $\varphi_m^j\left(x\right)$ are the Legendre polynomials of degree m on I_j. We further assume a Fourier solution of the form

$$u_m^j\left(t\right)=\beta_m e^{i(kx_j-\tilde{\omega}t)}, \tag{3.7}$$

where $\tilde{\omega}$ denotes the numerical angular frequency.

Substituting this ansatz into the semi-discrete DG formulation (2.3), choosing $\varphi_l^j\left(x\right)$ as v, and employing the upwind-biased numerical flux (2.4), we obtain

$$\tilde{\omega}\beta_l=\\ \frac{i\left(2l+1\right)}{h}\sum_{m=0}^{q}\left(\int_{-1}^{1}\varphi_m\varphi_l^{'}d\xi+\left(\theta+\left(1-\theta\right)e^{ikh}\left(-1\right)^m\right)\left(-1+e^{-ikh}\left(-1\right)^l\right)\right)\beta_m, \tag{3.8}$$

where $\varphi_l(\xi)$, $l=0,1,\cdots,q$, are Legendre polynomials defined on $[-1,1]$, which satisfy $\varphi_l(-1)=(-1)^l$, $\varphi_l(1)=1$ and $\int_{-1}^{1}\varphi_l(\xi)\,\varphi_m(\xi)\,d\xi=\frac{2}{2m+1}\,\delta_{lm}$, where δ_{lm} denotes the Kronecker delta. Let $\boldsymbol{\beta}=\left(\beta_0,\beta_1,\cdots,\beta_q\right)^{\mathrm{T}}$, then (3.8) can be written in matrix form as

$$\boldsymbol{A\beta}=\tilde{\omega}\boldsymbol{\beta}, \tag{3.9}$$

where the entries of the matrix $\boldsymbol{A}=(c_{lm})_{0\le l,m\le q}$ are given by

$$\boldsymbol{A}=\begin{bmatrix}c_{00}&c_{01}&\cdots&c_{0q}\\c_{10}&c_{11}&\cdots&c_{1q}\\\vdots&\vdots&\ddots&\vdots\\c_{q0}&c_{q1}&\cdots&c_{qq}\end{bmatrix},$$

and

$$c_{lm}=\frac{i\left(2l+1\right)}{h}\left(\int_{-1}^{1}\varphi_m\varphi_l^{'}d\xi+\left(\theta+\left(1-\theta\right)e^{ikh}\left(-1\right)^m\right)\left(-1+e^{-ikh}\left(-1\right)^l\right)\right).$$

The matrix $\boldsymbol{A}$ depends on the parameters θ, k, and h. For brevity, we emphasize its dependence on θ and denote $\boldsymbol{A} = \boldsymbol{A}(\theta)$. The numerical frequency $\tilde{\omega}$ adopts the same convention, and is written as $\tilde{\omega} = \tilde{\omega}(\theta)$. For a given θ, assume that $\boldsymbol{A}(\theta)$ has a complete set of eigenvectors. Then, according to the characteristic equation (3.9), $\tilde{\omega}(\theta)$ corresponds to an eigenvalue of $\boldsymbol{A}(\theta)$, with $\boldsymbol{\beta}$ being the associated eigenvector. Consequently, for each θ, the matrix $\boldsymbol{A}(\theta)$ possesses $q+1$ eigenvalues, which arise from the $q+1$ local degrees of freedom of the DG-P^q discretization. To analyze the propagation properties of the DG scheme, we denote $\tilde{\omega}(\theta) = \tilde{\omega}_r(\theta) + i\,\tilde{\omega}_i(\theta)$, where $\tilde{\omega}_r(\theta)$ governs the dispersive properties and $\tilde{\omega}_i(\theta)$ determines the dissipation. According to [1], the numerical solution of (3.2) are composed of $q+1$ waves and only the dispersion relation of the physical wave is close to that of the analytic solution.

To determine the optimal value of θ, we adopt two different optimization criteria based on dispersion properties.

The first criterion is based on minimizing the integrated error over a prescribed wavenumber range. Since very high wavenumbers are often underresolved and may dominate the integral without improving practical accuracy, we restrict the integration to representative cutoff wavenumbers. Specifically, we consider three cutoff values: $K_c = 0.6$ (well-resolved long-wave range), $K_c = 1.1$ (a broader usable band), and $K_c = \pi/2$ (a commonly used wide-band choice in DRP/CAA, corresponding to approximately half of the Nyquist limit). For a given cutoff wavenumber, (3.1) can be rewritten as

$$E(\theta; K_c) = \int_0^{K_c} |kh - \mathrm{Re}(\tilde{\omega}(\theta)\, h)|\ \mathrm{d}(kh), \tag{3.10}$$

which is a function of θ. The optimal value of θ is then obtained by solving the following optimization problem

$$\theta^* = \arg\min_{\theta} E(\theta; K_c). \tag{3.11}$$

According to the parameters K_c we have selected, we define the following three optimization rules, which will be denoted by $\mathbf{R_1}$-$\mathbf{R_3}$ in the subsequent analysis:

$$\begin{aligned} \mathbf{R_1}: &\quad \theta^* = \arg\min_{\theta} E(\theta; \pi/2), \\ \mathbf{R_2}: &\quad \theta^* = \arg\min_{\theta} E(\theta; 1.1), \\ \mathbf{R_3}: &\quad \theta^* = \arg\min_{\theta} E(\theta; 0.6). \end{aligned} \tag{3.12}$$

The second criterion follows the well-resolved wavenumber concept proposed in [1], which requires

$$|\mathrm{Re}\,(\tilde{\omega}h) - kh| < 0.01. \tag{3.13}$$

We define the corresponding optimization rule, denoted by $\mathbf{R_4}$, as selecting the value of θ that maximizes the well-resolved wavenumber range:

$$\mathbf{R_4}: \quad \theta^* = \arg\max_{\theta} K_r(\theta), \tag{3.14}$$

where

$$K_r(\theta) = \max\left\{K : |\mathrm{Re}(\tilde{\omega}(\theta)h) - kh| < 0.01, \forall kh \in (0, K)\right\}. \tag{3.15}$$

Here, we discretize the parameter θ with a sufficiently fine resolution and evaluate the dispersion relations for each discrete θ value using $\mathbf{R_1}$–$\mathbf{R_4}$ To ensure that different schemes employ the same number of degrees of freedom per wavelength, we denote h to represent one wavelength and $h_{DG-P^q} = (q+1)h$. The selected values of θ are summarized in Tab. 3.1 and the corresponding dispersion relations for these θ values are presented in Fig. 3.1, while the dissipation relations are shown in Fig. 3.2.

Tab. 3.1: Selected values of θ for the DG-P^q schemes by $\mathbf{R_1}$ to $\mathbf{R_4}$.

Scheme	$\mathbf{R_1}$	$\mathbf{R_2}$	$\mathbf{R_3}$	$\mathbf{R_4}$
DG-P^1	1.2167	1.1861	1.1579	1.2080
DG-P^2	1.3949	2.0000	0.8717	1.5203
DG-P^3	2.0000	0.7616	1.2512	0.7001
DG-P^4	0.7136	1.5641	2.0000	0.7076
DG-P^5	0.5972	2.0000	0.6692	1.2795

Tab. 3.2: Selected values of θ for the DG-P^q schemes.

Scheme	θ
DG-P^1	1.2167
DG-P^2	1.3949
DG-P^3	0.7001
DG-P^4	0.7136
DG-P^5	1.2795

To determine the optimal values of θ listed in Tab. 3.1, we compare the numerical dispersion curves obtained with different choices of θ with the exact dispersion relation. The optimal parameter is selected according to the agreement with the exact dispersion relation in the low-wavenumber range, as emphasized by the magnified inset in each figure. For the DG-P^1

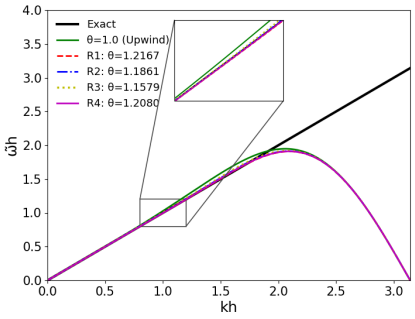

(a) DG-P^1

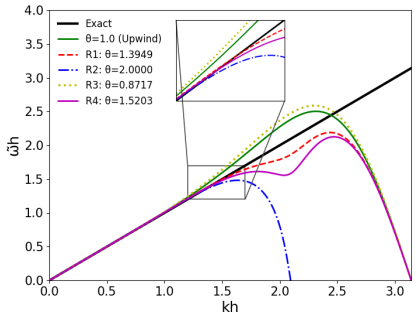

(b) DG-P^2

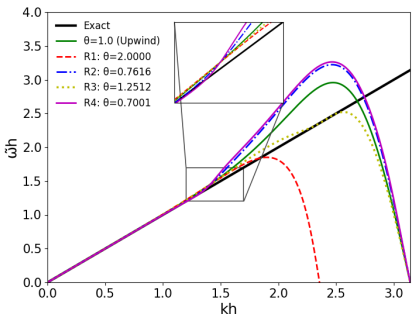

(c) DG-P^3

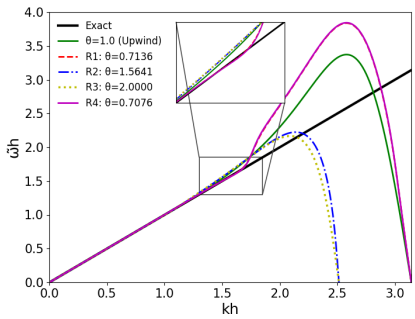

(d) DG-P^4

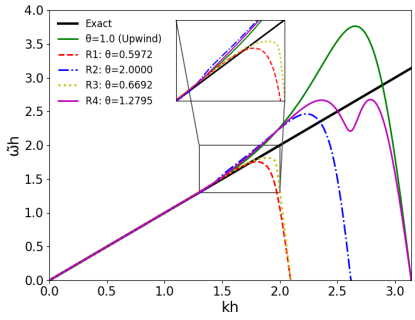

(e) DG-P^5

Fig. 3.1: Semi-discrete dispersion relations of the DG-P^q schemes for different values of θ.

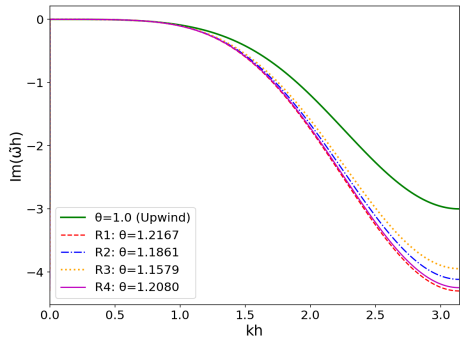

(a) DG-P^1

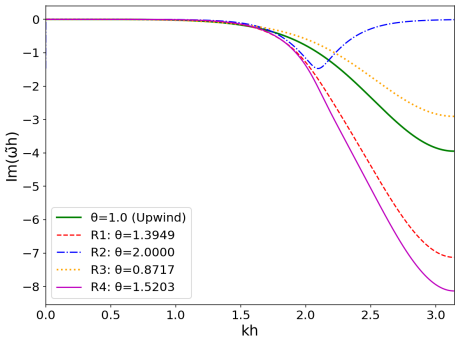

(b) DG-P^2

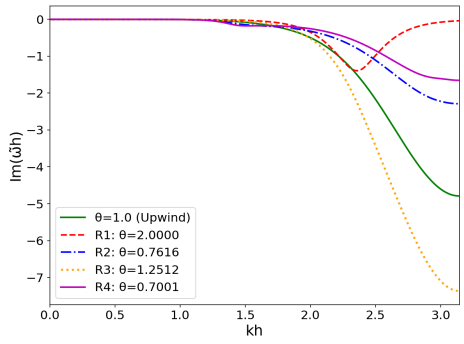

(c) DG-P^3

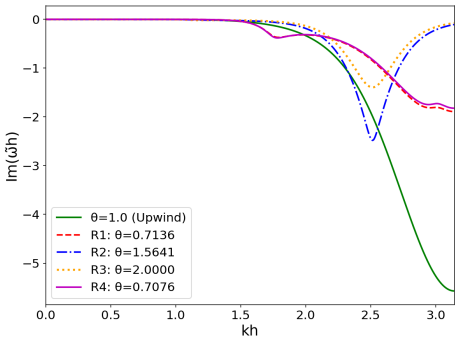

(d) DG-P^4

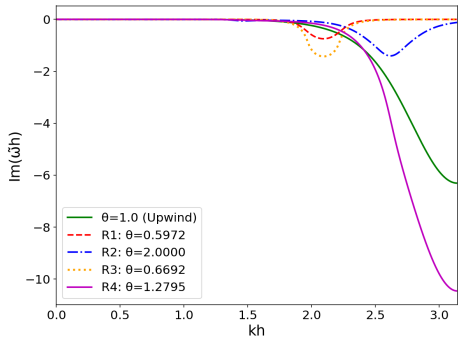

(e) DG-P^5

Fig. 3.2: Semi-discrete dissipation relations of the DG-P^q schemes for different values of θ.

scheme, as shown in Fig. 3.1a, $\theta = 1.2167$ improves the agreement with the exact curve compared with the standard choice $\theta = 1.0$. Applying the same criterion to higher-order schemes yields the optimal values $\theta = 1.3949$ (DG-P^2), $\theta = 0.7001$ (DG-P^3), $\theta = 0.7136$ (DG-P^4), and $\theta = 1.2795$ (DG-P^5), as shown in Fig. 3.1b–Fig. 3.1e.

Fig. 3.2 shows the dissipation relations corresponding to the values of θ selected primarily based on dispersion considerations. It is emphasized that the choice of θ in this study is not intended to minimize numerical dissipation. Instead, dissipation is examined to ensure that the dispersion-optimized parameters do not introduce excessive damping. We can also find that the numerical dissipation relations correspond to the values of θ, with stronger dissipation observed for larger θ.

Overall, the analysis confirms that the proposed selection of θ prioritizes dispersion relations rather than dissipation minimization. The resulting schemes achieve improved dispersion behavior over the dominant wavenumber range, while the associated dissipation remains at an acceptable level. Although smaller dissipation could be achieved for other choices of θ, such values may compromise the dispersion properties or lead to undesirable numerical behavior. Therefore, the selected values represent a balanced compromise, guided primarily by dispersion considerations, and are adopted in the subsequent numerical experiments.

3.2 Dispersion and Dissipation Error

In [3], the dispersion and dissipation properties of DG schemes with upwind-biased fluxes were investigated through the physically relevant eigenmode of the semi-discrete operator for general values of the flux parameter θ, and a small-mesh asymptotic expansion of the physical eigenvalue was derived to characterize the leading-order dispersion and dissipation errors. In contrast, the present work substitutes the dispersion-optimized parameters identified in the previous section into this general framework and examines the corresponding asymptotic behavior of the physical eigenmode. To adopt the same analytical framework, we introduce the dimensionless quantities

$$K = kh, \qquad \omega^* = \tilde{\omega} h, \tag{3.16}$$

where K denotes the dimensionless wavenumber and ω^* denotes the dimensionless numerical frequency. In terms of these variables, the expansion of the physical eigenmode corresponds to a Taylor series around $K = 0$ of the form

$$\omega^* = \omega_r^* + i\omega_i^*, \tag{3.17}$$

where

$$\begin{aligned} \omega_r^* &= K + C_1 K^{2q+3} + \mathcal{O}(K^{2q+5}), \\ \omega_i^* &= C_2 K^{2q+2} + \mathcal{O}(K^{2q+4}), \end{aligned} \tag{3.18}$$

and the coefficients C_1 and C_2 characterize the leading-order dispersion and dissipation errors, respectively. Here ω_r^* and ω_i^* represent the dispersion and dissipation properties of the physical eigenmode, respectively. Building on this approach, we perform the same local eigenmode expansion for DG schemes equipped with the dispersion-optimized parameters identified in the preceding section. For polynomial degrees $q = 1$ to $q = 5$, the Taylor expansions of the physical eigenmode around $K = 0$ are given as follows.

$$q = 1 : \begin{cases} \theta = 1.0 : \begin{cases} \omega_r^* = K + 3.70 \times 10^{-3} K^5 + \mathcal{O}(K^7), \\ \omega_i^* = -1.39 \times 10^{-2} K^4 + \mathcal{O}(K^8), \end{cases} \\ \theta = 1.2167 : \begin{cases} \omega_r^* = K - 1.05 \times 10^{-3} K^5 + \mathcal{O}(K^7), \\ \omega_i^* = -9.69 \times 10^{-3} K^4 + \mathcal{O}(K^8), \end{cases} \end{cases} \tag{3.19}$$

$$q = 2 : \begin{cases} \theta = 1.0 : \begin{cases} \omega_r^* = K + 2.38 \times 10^{-4} K^7 + \mathcal{O}(K^9), \\ \omega_i^* = -1.39 \times 10^{-4} K^6 + \mathcal{O}(K^8), \end{cases} \\ \theta = 1.3949 : \begin{cases} \omega_r^* = K + 2.07 \times 10^{-4} K^7 + \mathcal{O}(K^9), \\ \omega_i^* = -2.49 \times 10^{-4} K^6 + \mathcal{O}(K^8), \end{cases} \end{cases} \tag{3.20}$$

$$q = 3 : \begin{cases} \theta = 1.0 : \begin{cases} \omega_r^* = K + 9.00 \times 10^{-8} K^9 + \mathcal{O}(K^{11}), \\ \omega_i^* = -7.09 \times 10^{-7} K^8 + \mathcal{O}(K^{10}), \end{cases} \\ \theta = 0.7001 : \begin{cases} \omega_r^* = K + 2.21 \times 10^{-6} K^9 + \mathcal{O}(K^{11}), \\ \omega_i^* = -1.77 \times 10^{-6} K^8 + \mathcal{O}(K^{10}), \end{cases} \end{cases} \tag{3.21}$$

$$q = 4 : \begin{cases} \theta = 1.0 : \begin{cases} \omega_r^* = K + 4.53 \times 10^{-9} K^{11} + \mathcal{O}(K^{13}), \\ \omega_i^* = -4.57 \times 10^{-8} K^{10} + \mathcal{O}(K^{12}), \end{cases} \\ \theta = 0.7136 : \begin{cases} \omega_r^* = K - 7.72 \times 10^{-10} K^{11} + \mathcal{O}(K^{13}), \\ \omega_i^* = -9.34 \times 10^{-10} K^{10} + \mathcal{O}(K^{12}), \end{cases} \end{cases} \tag{3.22}$$

$$q = 5 : \begin{cases} \theta = 1.0 : \begin{cases} \omega_r^* = K + 2.64 \times 10^{-12} K^{13} + \mathcal{O}(K^{15}), \\ \omega_i^* = -2.21 \times 10^{-11} K^{12} + \mathcal{O}(K^{14}), \end{cases} \\ \theta = 1.2795 : \begin{cases} \omega_r^* = K - 1.07 \times 10^{-12} K^{13} + \mathcal{O}(K^{15}), \\ \omega_i^* = -2.90 \times 10^{-12} K^{12} + \mathcal{O}(K^{14}). \end{cases} \end{cases} \tag{3.23}$$

Tab. 3.3 is constructed by comparing the leading-order dispersion and dissipation error coefficients appearing in (3.19)–(3.23) for the upwind-biased

and standard upwind numerical fluxes. It can be seen that in most cases the leading error coefficients of the optimized schemes are smaller than those of the standard upwind schemes. The error orders obtained here are consistent with the theoretical results reported in [3]. In particular, the physical mode satisfies the expected asymptotic behavior shown in 3.18, demonstrating that the schemes correctly capture the physical wave speed at low wavenumbers.

Tab. 3.3: Comparison of the leading-order dispersive and dissipative error coefficients between optimized upwind-biased fluxes and the standard upwind flux for different DG schemes.

DG scheme	Scheme with smaller dispersion error	Scheme with smaller dissipation error
DG-P^1	**optimized**	**optimized**
DG-P^2	**optimized**	**upwind**
DG-P^3	**upwind**	**upwind**
DG-P^4	**optimized**	**optimized**
DG-P^5	**optimized**	**optimized**

4 Application to One-Dimensional Linear Systems

In this section, the optimal dispersion parameters derived in Sec. 2 for scalar problems are applied to one-dimensional linear systems. Our objective is to examine whether the conclusions obtained for the scalar advection equation remain applicable when the DG method is applied to linear hyperbolic systems.

Following [12], the Lax-Friedrichs flux is commonly adopted as the numerical flux for DG discretizations of linear systems. To facilitate the application of the optimal dispersion parameters obtained earlier, we first diagonalize the linear system and reformulate it as a set of independent scalar equations. These decoupled equations are then discretized using the DG method with upwind and upwind-biased numerical fluxes. We consider a simple linear system:

$$\boldsymbol{u}_t + \boldsymbol{f}\left(\boldsymbol{u}\right)_x = \boldsymbol{0}, \quad \boldsymbol{f}\left(\boldsymbol{u}\right) = \boldsymbol{A}\boldsymbol{u},\ \boldsymbol{A} \in \mathbb{R}^{m\times m}, \tag{4.1}$$

where $\boldsymbol{u} = \left(u_1, u_2 \cdots, u_m\right)^{\mathrm{T}}$, $\boldsymbol{A}$ is a diagonalizable constant matrix. The DG method for solving (4.1) is given as follows:

$$\int_{I_j} \left(\boldsymbol{u_h}\right)_t \varphi dx = \int_{I_j} \boldsymbol{f}\left(\boldsymbol{u_h}\right) \varphi_x dx - \left(\hat{\boldsymbol{f}}_{j+\frac{1}{2}} \varphi^-_{j+\frac{1}{2}} - \hat{\boldsymbol{f}}_{j-\frac{1}{2}} \varphi^+_{j-\frac{1}{2}}\right), \tag{4.2}$$

where $\boldsymbol{u_h} = (u_{1,h}, u_{2,h} \cdots, u_{m,h})^{\mathrm{T}} \in [V_h^q]^m$ is the numerical solution vector, $\varphi \in V_h^q$ is a test function, and $\hat{\boldsymbol{f}}$ is taken as the Lax-Friedrichs flux:

$$\hat{\boldsymbol{f}}^{LF}(\boldsymbol{u}^-, \boldsymbol{u}^+) = \frac{1}{2}\left(\boldsymbol{f}(\boldsymbol{u}^+) + \boldsymbol{f}(\boldsymbol{u}^-)\right) - \frac{\alpha}{2}\left(\boldsymbol{u}^+ - \boldsymbol{u}^-\right), \tag{4.3}$$

where $\alpha = \max\left(|\lambda_1|, |\lambda_2|, \cdots, |\lambda_m|\right)$, and λ_p is the p-th eigenvalues of the Jacobian matrix $\frac{\partial \boldsymbol{f}}{\partial \boldsymbol{u}} = \boldsymbol{A}$.

In order to employ our scheme, we perform an eigenvalue decomposition of coefficient matrix $\boldsymbol{A}$. Then there exists an invertible matrix $\boldsymbol{R}$ and a diagonal matrix $\boldsymbol{\Lambda} = \mathrm{diag}\left(\lambda_1, \lambda_2, \cdots, \lambda_m\right)$, such that $\boldsymbol{A} = \boldsymbol{R\Lambda R^{-1}}$. Furthermore, defining $\boldsymbol{R^{-1}u} = \boldsymbol{v} = (v_1, v_2 \cdots, v_m)^{\mathrm{T}}$ and multiplying both sides of (4.1) from the left by $\boldsymbol{R}^{-1}$, we obtain a system consisting of independent scalar equations

$$\boldsymbol{v}_t + \boldsymbol{\Lambda v}_x = \boldsymbol{0}. \tag{4.4}$$

That is, the original linear system is transformed into a set of independent scalar equations, each associated with an eigenvalue λ_i. Then, we solve (4.4) using the following DG method:

$$\int_{I_j} (\boldsymbol{v}_h)_t \varphi \, dx = \int_{I_j} \boldsymbol{g}(\boldsymbol{v}_h)\varphi_x \, dx - \left(\hat{\boldsymbol{g}}^{up-bia}_{j+\frac{1}{2}} \varphi^-_{j+\frac{1}{2}} - \hat{\boldsymbol{g}}^{up-bia}_{j-\frac{1}{2}} \varphi^+_{j-\frac{1}{2}}\right), \tag{4.5}$$

where

$$\boldsymbol{v}_h = (v_{1,h}, v_{2,h}, \cdots, v_{m,h})^{\mathrm{T}}, \qquad \boldsymbol{g}(\boldsymbol{v}) = \boldsymbol{\Lambda v}.$$

And $\hat{\boldsymbol{g}}^{up-bia}$ is the upwind-biased flux, given as

$$\hat{\boldsymbol{g}}^{up-bia}(\boldsymbol{v}^-, \boldsymbol{v}^+) = \frac{\boldsymbol{\Lambda}}{2}\left(\boldsymbol{v}^+ + \boldsymbol{v}^-\right) - \frac{\boldsymbol{D'}}{2}\left(\boldsymbol{v}^+ - \boldsymbol{v}^-\right), \tag{4.6}$$

with $\boldsymbol{D'} = (2\theta - 1)\,\mathrm{diag}\left(|\lambda_1|, |\lambda_2|, \cdots, |\lambda_m|\right)$. We can transform this numerical flux back to the one corresponding to the original conservative variables $\boldsymbol{u}_h$,

$$\hat{\boldsymbol{f}}^{up-bia}(\boldsymbol{u}^-, \boldsymbol{u}^+) = \frac{\boldsymbol{A}}{2}\left(\boldsymbol{u}^+ + \boldsymbol{u}^-\right) - \frac{\boldsymbol{RD'R^{-1}}}{2}\left(\boldsymbol{u}^+ - \boldsymbol{u}^-\right). \tag{4.7}$$

In the numerical simulation, we will employ the DG scheme (4.2) with numerical flux (4.7).

In summary, by diagonalizing the one-dimensional linear system, the original system is transformed into a set of independent scalar equations. This approach naturally facilitates the application of upwind-biased numerical

fluxes to each scalar component, allowing the optimal dispersion parameter θ, originally derived for scalar problems, to be directly employed in the system setting. In the following numerical experiments in Sec. 5, the resulting upwind-biased DG schemes are compared with the standard DG method using the Lax–Friedrichs flux to assess their dispersion and dissipation properties.

5 Numerical Experiments

In this section, a series of numerical experiments are presented to verify the theoretical results derived in Sec. 3 and Sec. 4. In particular, we focus on validating the dispersion properties of the proposed DG schemes with optimally chosen upwind-biased flux parameters. Although the theoretical analysis in this paper is carried out for constant coefficient linear problems, several numerical experiments involving geometric source terms are also included. These tests are intended to assess the practical performance of the proposed DG schemes beyond the scope of the theoretical analysis.

Example 5.1. To assess the performance of the schemes obtained in Sec. 3, which are designed to achieve optimal dispersion relations for polynomial degrees $q = 1$ to $q = 5$, we consider the following linear convection equation:

$$\begin{cases} u_t + u_x = 0, \\ u\left(x, 0\right) = \frac{1}{2} e^{-(\ln 2)\left(\frac{x}{2}\right)^2}, \end{cases} \tag{5.1}$$

with analytic solution

$$u\left(x, t\right) = \frac{1}{2} e^{-(\ln 2)\left(\frac{x-t}{2}\right)^2}. \tag{5.2}$$

A sufficiently large computational region $[-800, 1000]$ is selected to allow compactly supported boundary conditions. In order to ensure the same number of degrees of freedom per wavelength for all schemes, we let $h_{DG-P^q} = q + 1$, the time step is set to $\Delta t = \frac{1}{30} h_{DG-P^q}$. In the DG schemes with upwind-biased numerical fluxes, the parameter θ is selected according to the optimal values derived in Sec. 3. For comparison, the standard upwind flux with $\theta = 1.0$ is also used. Time integration is carried out using the third-order strong stability preserving Runge–Kutta method, and the numerical solutions are computed up to $t = 400$. The numerical solutions obtained with different DG schemes are displayed in Fig. 5.1, where the exact solutions are shown for reference. Quantitative comparisons are provided in Tab.

5.1, which lists the L^1, L^2, and L^∞ errors between the numerical and exact solutions.

From these figures, we can see that the DG schemes with the proposed upwind-biased fluxes perform better than those using the standard upwind flux. The use of the optimized θ values leads to visibly improved agreement with the exact solution, which is further quantified by the smaller L^1, L^2, and L^∞ errors reported in Tab. 5.1. This consistent error reduction demonstrates the advantage of the proposed flux choice and confirms the theoretical results.

Tab. 5.1: L^1, L^2, L^∞ errors between the numerical and exact solutions for DG-P^q with different θ values in **Example 5.1.**

Method	$\boldsymbol{\theta}$ **values**	L^1	L^2	L^∞
DG-P^1	$\theta = 1.0000$	1.0735e-03	1.1827e-02	2.7686e-01
	$\theta = 1.2167$	1.0197e-03	1.1301e-02	2.6298e-01
	Reduction (%)	5.01	4.45	5.01
DG-P^2	$\theta = 1.0000$	6.0660e-04	6.7976e-03	1.5313e-01
	$\theta = 1.3949$	5.9912e-04	6.7580e-03	1.4668e-01
	Reduction (%)	1.23	0.58	4.21
DG-P^3	$\theta = 1.0000$	3.7007e-04	4.1243e-03	9.1009e-02
	$\theta = 0.7001$	2.8947e-04	3.1709e-03	6.9359e-02
	Reduction (%)	21.78	23.11	23.79
DG-P^4	$\theta = 1.0000$	2.5224e-04	2.7383e-03	6.3824e-02
	$\theta = 0.7136$	2.5177e-04	2.8325e-03	6.1654e-02
	Reduction (%)	0.19	-3.44	3.40
DG-P^5	$\theta = 1.0000$	1.8360e-04	2.0365e-03	4.9136e-02
	$\theta = 1.2795$	1.5966e-04	1.8171e-03	4.5102e-02
	Reduction (%)	13.04	10.78	8.21

Example 5.2. In this example, we investigate the aliasing effects for the linear convective wave equation in [29]

$$u_t + u_x = 0, \tag{5.3}$$

subject to the initial condition

$$u(x,0) = (2 + \cos(\alpha x))\, e^{-(\ln 2)\left(\frac{x}{10}\right)^2}. \tag{5.4}$$

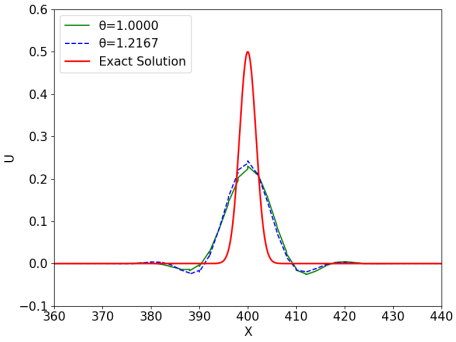

(a) DG-P^1

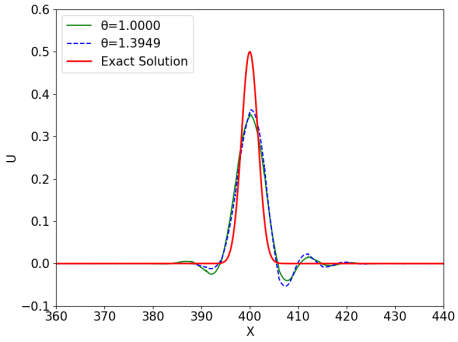

(b) DG-P^2

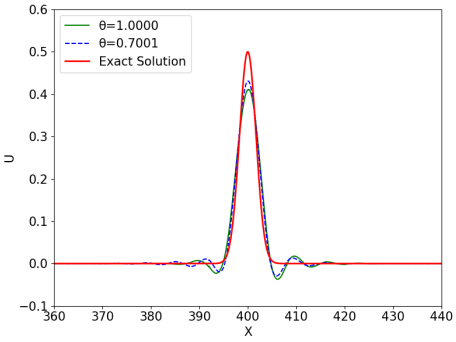

(c) DG-P^3

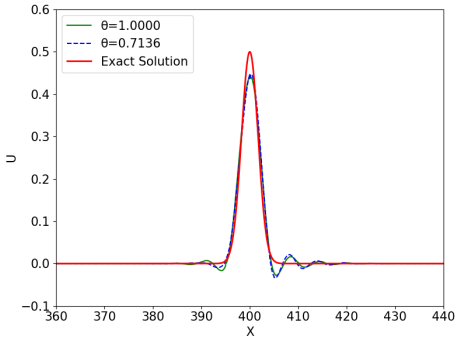

(d) DG-P^4

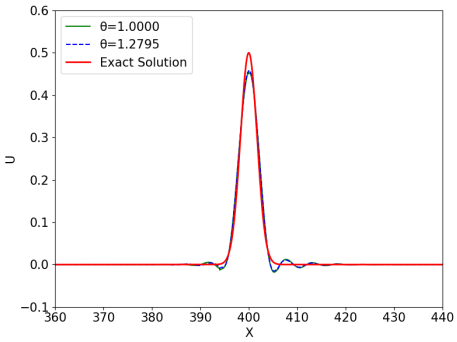

(e) DG-P^5

Fig. 5.1: Comparisons between numerical solutions obtained using the standard upwind flux and the optimized upwind-biased flux for DG-P^q schemes ($q = 1, 2, 3, 4, 5$), $h_{DG-P^q} = q + 1$. The exact solution is shown for reference.

where the wavenumber $\alpha = 1.7$ is considered. This value corresponds to a higher-frequency mode that is under-resolved on the given mesh and therefore induces aliasing errors. The exact solution is given by

$$u(x,t) = \big(2 + \cos\big(\alpha(x-t)\big)\big)\, e^{-(\ln 2)\left(\frac{x-t}{10}\right)^2}. \tag{5.5}$$

The problem is solved using the DG-P^4 and DG-P^5 schemes. Fig. 5.2 compares the numerical and exact solutions at $t = 800$. The corresponding L^1, L^2, and L^∞ errors obtained with the standard upwind flux ($\theta = 1.0$) and the optimized upwind-biased flux are reported in Tab. 5.2. As shown in Table, the DG scheme employing the optimized θ value consistently produces smaller errors. This indicates that, even in the presence of aliasing effects, the optimized upwind-biased flux provides slightly improved performance compared with the standard upwind flux.

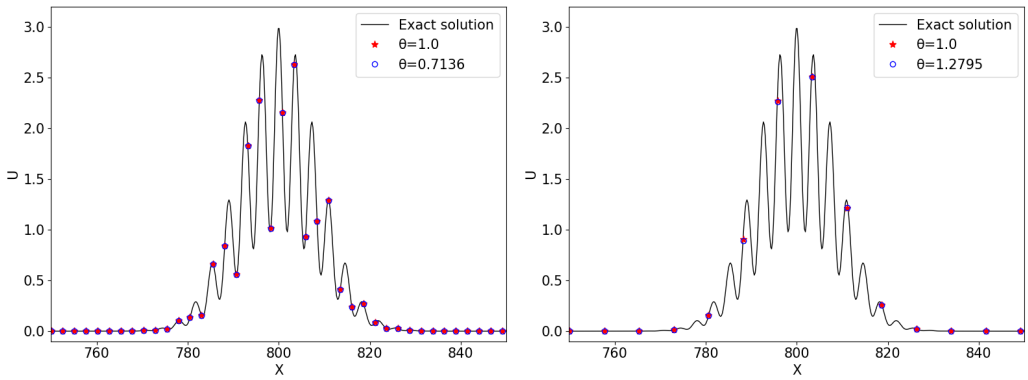

(a) $N = 1200$, DG-P^4 **(b)** $N = 400$, DG-P^5

Fig. 5.2: Numerical and exact solutions for the aliasing test obtained with the DG-P^4 and DG-P^5 schemes, the mesh sizes are chosen according to N. Here N denotes the number of cells, and the CFL number is set to 1/30.

Tab. 5.2: L^1, L^2, L^∞ errors between the numerical and exact solutions for DG-P^q with different θ values in **Example 5.2.**

Method	$\boldsymbol{\theta}$ **values**	L^1	L^2	L^∞
DG-P^4	$\theta = 1.0000$	8.7508e-05	5.6247e-04	6.7969e-03
	$\theta = 0.7136$	8.7200e-05	5.6052e-04	6.6365e-03
	Reduction (%)	0.35	0.35	2.36
DG-P^5	$\theta = 1.0000$	2.6399e-03	1.7069e-02	2.0515e-01
	$\theta = 1.2795$	2.6280e-03	1.6931e-02	2.0210e-01
	Reduction (%)	0.45	0.81	1.49

Example 5.3. In this example, we consider a spherical wave propagation problem in [30], which is governed by the one-dimensional equation

$$\frac{\partial u}{\partial t} + \frac{u}{r} + \frac{\partial u}{\partial r} = 0, \tag{5.6}$$

where the term u/r accounts for the geometric spreading effect. The computational domain is chosen as $[5, 450]$, and a time-dependent boundary condition is prescribed at $r = 5$

$$u(5, t) = \sin(\omega t), \tag{5.7}$$

where $\omega = \pi/3$ is used in the simulations. The exact solution of this problem is given by

$$u(r, t) = \frac{5}{r}\,\sin\big(\omega(t - r + 5)\big). \tag{5.8}$$

Numerical solutions are computed using the DG-P^1 and DG-P^2 schemes and examined at $t = 100$, 200, 300, and 400. Fig. 5.3 and Fig. 5.4 show the corresponding results. Tab. 5.3 and 5.4 show the L^1, L^2, and L^∞ errors at different times for both the standard upwind flux and the optimized upwind-biased flux. It is observed that the optimized choice of θ consistently yields smaller errors than the standard upwind flux for all reported times. These results demonstrate that the dispersion-optimized flux remains effective for problems involving geometric source terms and time dependent boundary conditions.

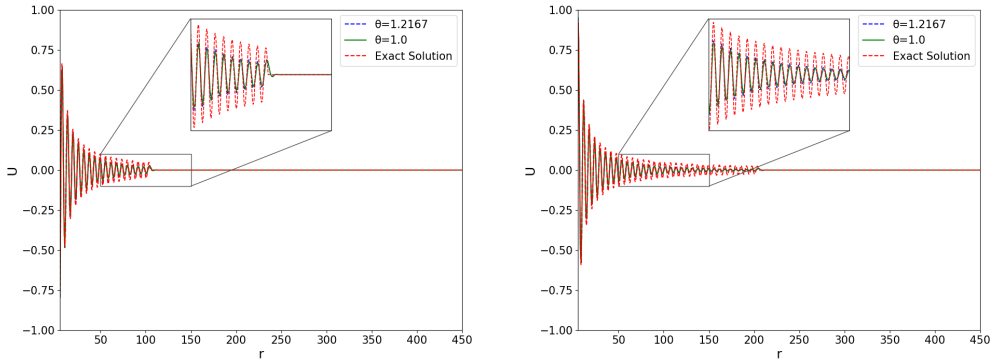

(a) $t = 100$ **(b)** $t = 200$

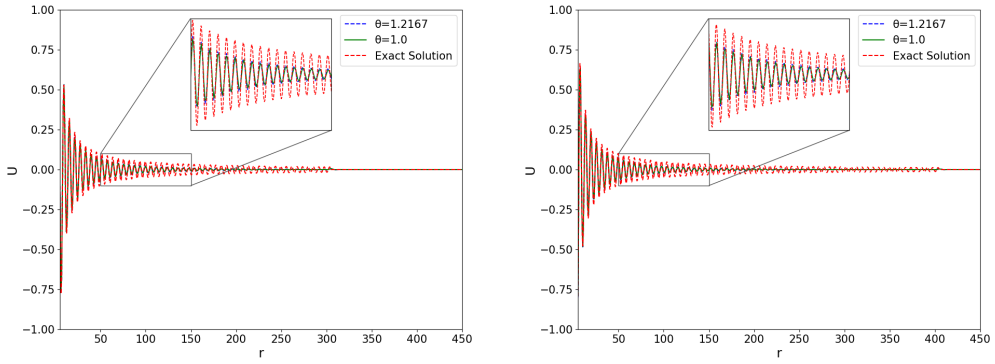

(c) $t = 300$ **(d)** $t = 400$

Fig. 5.3: Numerical and exact solutions at $t = 100, 200, 300$, and 400 with $\omega = \pi/3$, obtained using the DG-P^1 scheme on a uniform mesh with $N = 500$ cells. The CFL number is set to $1/30$.

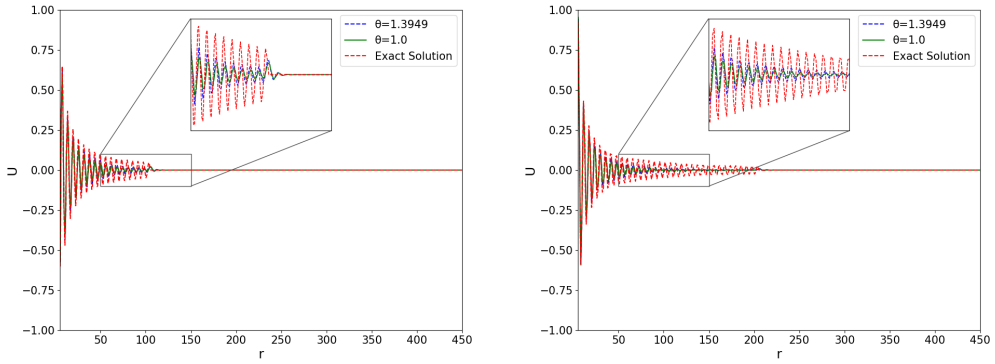

(a) $t = 100$ **(b)** $t = 200$

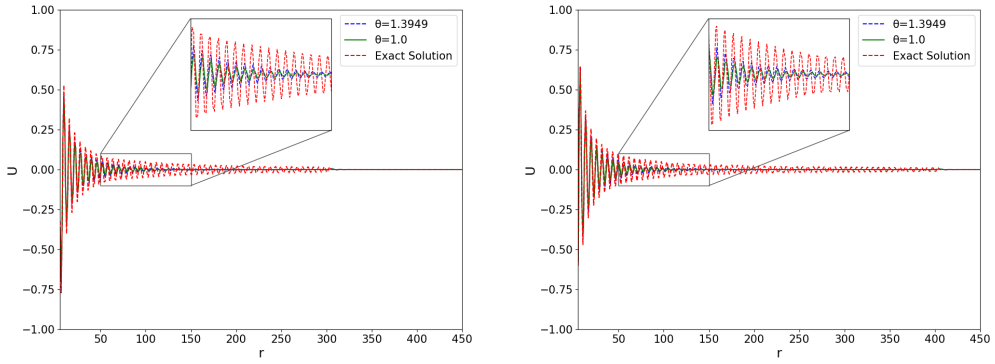

(c) $t = 300$ **(d)** $t = 400$

Fig. 5.4: Numerical and exact solutions at $t = 100, 200, 300$, and 400 with $\omega = \pi/3$, obtained using the DG-P^2 scheme on a uniform mesh with $N = 150$ cells. The CFL number is set to $1/30$.

Tab. 5.3: L^1, L^2, and L^∞ errors for the spherical wave problem in **Example 5.3.** obtained with the DG-P^1 scheme ($N = 500$) using the standard upwind flux and the optimized upwind-biased flux.

t	Error	$\theta = 1.2167$	$\theta = 1.0$	Reduction (%)
$t = 100$	L^1	4.5302e-03	5.2965e-03	14.47
	L^2	1.0686e-02	1.2498e-02	14.50
	L^∞	3.8926e-02	4.4350e-02	12.23
$t = 200$	L^1	7.9770e-03	9.1298e-03	12.63
	L^2	1.3469e-02	1.5471e-02	12.94
	L^∞	5.8939e-02	5.9218e-02	0.47
$t = 300$	L^1	1.0504e-02	1.1833e-02	11.23
	L^2	1.4735e-02	1.6752e-02	12.04
	L^∞	5.1988e-02	6.2973e-02	17.44
$t = 400$	L^1	1.2407e-02	1.3785e-02	9.99
	L^2	1.5358e-02	1.7326e-02	11.36
	L^∞	3.8926e-02	4.4350e-02	12.23

Tab. 5.4: L^1, L^2, and L^∞ errors for the spherical wave problem in **Example 5.3.** obtained with the DG-P^2 scheme ($N = 150$) using the standard upwind flux and the optimized upwind-biased flux.

t	Error	$\theta = 1.3949$	$\theta = 1.0$	Reduction (%)
$t = 100$	L^1	7.7008e-03	9.6190e-03	19.94
	L^2	1.8309e-02	2.3053e-02	20.58
	L^∞	7.6355e-02	9.6954e-02	21.25
$t = 200$	L^1	1.3014e-02	1.5304e-02	14.97
	L^2	2.2378e-02	2.7163e-02	17.61
	L^∞	1.7695e-01	2.0275e-01	12.72
$t = 300$	L^1	1.6068e-02	1.8130e-02	11.38
	L^2	2.3717e-02	2.8072e-02	15.51
	L^∞	1.1431e-01	1.4082e-01	18.82
$t = 400$	L^1	1.7538e-02	1.9469e-02	9.92
	L^2	2.3169e-02	2.7211e-02	14.86
	L^∞	7.6342e-02	9.6943e-02	21.25

Example 5.4. In this example, we consider a linear hyperbolic system,

namely the one-dimensional linearized Euler equations without mean flow

$$\begin{cases} u_t + p_x = 0, \\ p_t + u_x = 0, \end{cases} \tag{5.9}$$

with the initial conditions

$$\begin{cases} u(x,0) = e^{-(\ln 2)\left(\frac{x}{b}\right)^2}, \\ p(x,0) = 0. \end{cases} \tag{5.10}$$

The exact solution of (5.9) can be expressed as a superposition of left- and right-traveling waves,

$$\begin{cases} u(x,t) = \dfrac{1}{2}\left[u(x-t,0) + u(x+t,0)\right], \\ p(x,t) = \dfrac{1}{2}\left[u(x-t,0) - u(x+t,0)\right]. \end{cases} \tag{5.11}$$

A sufficiently large computational domain $[-420,\ 420]$ is adopted. Let $h_{DG-P^q} = q+1$, $\Delta t = \frac{1}{30} h_{DG-P^q}$. For each scheme, the same mesh size h (or equivalently h_{DG-P^q}) is used for both the Lax–Friedrichs flux and the upwind-biased flux. Since the solution consists of two counter-propagating waves, numerical results are examined at $t = 400$. Both the Lax-Friedrichs flux and the optimized upwind-biased flux are used in the DG discretization. Fig. 5.5 presents the numerical solutions obtained with the DG-P^q schemes for different polynomial degrees, and quantitative comparisons are given in Tab. 5.5. It is observed that consistent with the scalar case, the DG schemes equipped with the optimized upwind-biased flux provide better results than those obtained using the Lax-Friedrichs flux.

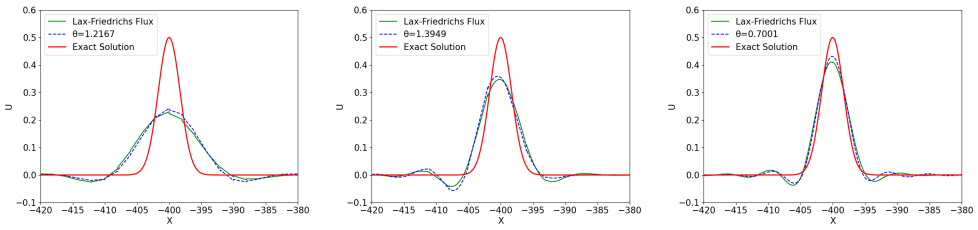

(a) DG-P^1 **(b)** DG-P^2 **(c)** DG-P^3

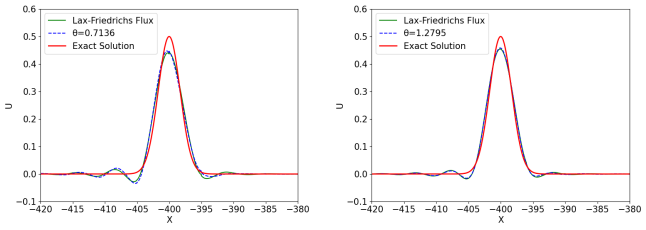

(d) DG-P^4 **(e)** DG-P^5

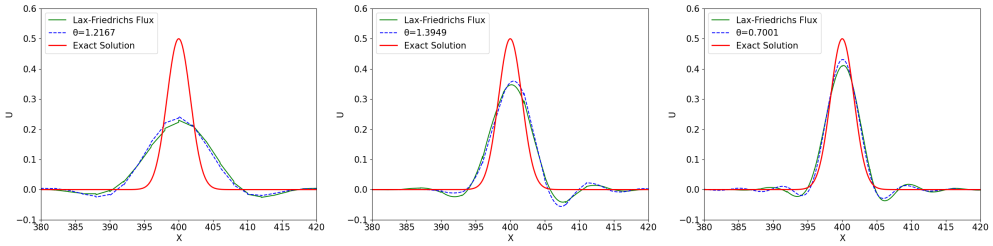

(f) DG-P^1 **(g)** DG-P^2 **(h)** DG-P^3

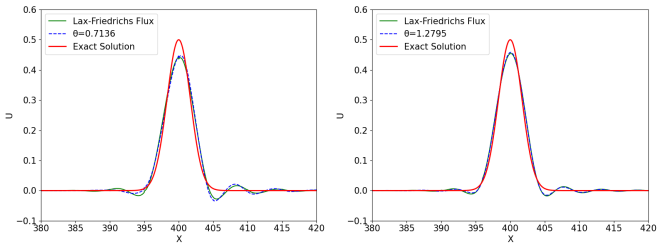

(i) DG-P^4 **(j)** DG-P^5

Fig. 5.5: Comparisons between numerical and exact solutions for the linearized Euler system in **Example 5.4** obtained using the Lax-Friedrichs flux and the optimized upwind-biased flux with DG-P^q schemes ($q = 1, 2, 3, 4, 5$), $h_{DG-P^q} = q + 1$. Figures (a)–(e) correspond to the upstream region with $x \in [-420, -380]$, while figures (f)–(j) correspond to the downstream region with $x \in [380, 420]$.

Tab. 5.5: L^1, L^2, and L^∞ errors for the linearized Euler system in **Example 5.4.** obtained using DG-P^q schemes with the standard upwind flux and the optimized upwind-biased fluxes.

Method	$\boldsymbol{\theta}$ **values**	L^1	L^2	L^∞
DG-P^1	Lax-Friedrichs Flux	4.5707e-03	2.4483e-02	2.7704e-01
	$\theta = 1.2167$	4.3547e-03	2.3394e-02	2.6313e-01
	Reduction (%)	4.73	4.45	5.02
DG-P^2	Lax-Friedrichs Flux	2.6143e-03	1.4075e-02	1.5087e-01
	$\theta = 1.3949$	2.5180e-03	1.3996e-02	1.4117e-01
	Reduction (%)	3.68	0.56	6.43
DG-P^3	Lax-Friedrichs Flux	1.5739e-03	8.5376e-03	8.9972e-02
	$\theta = 0.7001$	1.2363e-03	6.5641e-03	6.8827e-02
	Reduction (%)	21.45	23.11	23.50
DG-P^4	Lax-Friedrichs Flux	1.0695e-03	5.6682e-03	5.8911e-02
	$\theta = 0.7136$	1.0688e-03	5.8632e-03	5.7461e-02
	Reduction (%)	0.07	-3.44	2.46
DG-P^5	Lax-Friedrichs Flux	7.8360e-04	4.2387e-03	4.5573e-02
	$\theta = 1.2795$	6.8350e-04	3.7881e-03	4.1554e-02
	Reduction (%)	12.77	10.63	8.82

Example 5.5. The propagation of sound waves through a transonic nozzle is a classical problem in [28]. Accurate numerical simulation of acoustic waves in such configurations is challenging due to the strong coupling between mean flow variations and acoustic perturbations. In this example, we consider a one-dimensional acoustic wave transmission problem through a nearly choked nozzle.

The characteristic scales used in this study are defined as follows:

- Length scale: D, the diameter of the duct in the uniform region upstream of the nozzle;
- Velocity scale: a_r, the speed of sound in the same region;
- Time scale: D/a_r;
- Density scale: ρ_r, the mean density in the upstream uniform region;
- Pressure scale: $\rho_r a_r^2$.

The governing equations are the quasi-one-dimensional compressible linear Euler equations,

$$\frac{\partial \rho'}{\partial t} + \frac{\bar{\rho} u'}{A}\frac{dA}{dx} + \bar{\rho}\frac{\partial u'}{\partial x} + u'\frac{d\bar{\rho}}{dx} + \rho'\frac{\bar{u}}{A}\frac{dA}{dx} + \rho'\frac{d\bar{u}}{dx} + \bar{u}\frac{\partial \rho'}{\partial x} = 0, \tag{5.12}$$

$$\bar{\rho}\frac{\partial u'}{\partial t} + \rho'\bar{u}\frac{\partial u'}{\partial x} + \rho'\bar{u}\frac{d\bar{u}}{dx} + \bar{\rho}u'\frac{d\bar{u}}{dx} + \frac{\partial p'}{\partial x} = 0, \tag{5.13}$$

$$\frac{\partial p'}{\partial t} + \bar{u}\frac{\partial p'}{\partial x} + u'\frac{d\bar{p}}{dx} + \frac{\gamma}{A}\left(\bar{p}u' + p'\bar{u}\right)\frac{dA}{dx} + \gamma\bar{p}\frac{\partial u'}{\partial x} + \gamma p'\frac{d\bar{u}}{dx} = 0, \tag{5.14}$$

where $\gamma = 1.4$ and $A(x) = \pi R(x)^2$ is the cross-sectional area of the nozzle. The nozzle geometry is illustrated in Fig. 5.6, and the radius function $R(x)$ is prescribed piecewise as

$$R(x) = \begin{cases} 0.5, & x < -0.4, \\ -24.5571(x+0.4)^4 + 26.1942(x+0.4)^3 \\ \quad -7.8586(x+0.4)^2 + 0.5, & -0.4 \le x \le 0, \\ -0.0265(x+0.4)^4 + 0.0991(x+0.4)^3 \\ \quad -0.0934(x+0.4)^2 + 0.0340(x+0.4) & 0 < x \le 1.6, \\ \quad +0.2861, \\ 0.3484, & x > 1.6. \end{cases}$$

We set the upstream uniform-flow parameters as $A_r = \pi/4$, $\rho_r = 1$, $u_r = M_r = 0.2$, and $p_r = 1/\gamma$, and take the computational domain $[-1.2, 2.2]$. The method described in Sec. 4 will be used to compute this problem with the DG-P^2 scheme and $N = 480$.

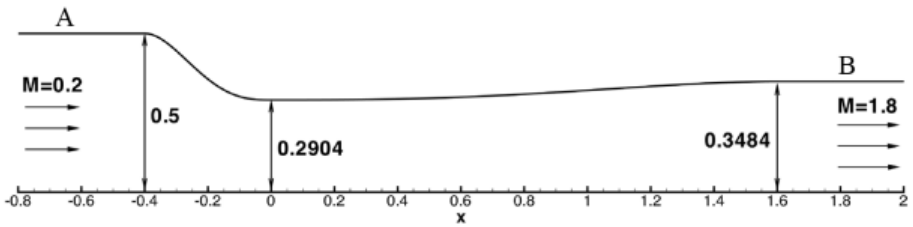

Fig. 5.6: Geometry of supersonic nozzle

An entropy wave pulse is imposed at $t = 0$,

$$\rho' = 0.001 \exp\left(- (\ln 2) \left(\frac{x - x_0 - \bar{u}t}{3\Delta/(q_0 + 1)} \right)^2 \right), \tag{5.15}$$

$$p' = 0, \tag{5.16}$$

$$u' = 0, \tag{5.17}$$

where x_0 denotes the left boundary of the computational domain, $\bar{u} = u_r$, Δ is the mesh spacing, which depends on the number of mesh cells N and $q_0 = 2$. The steady mean flow is computed using a Newton iteration. The resulting mean flow profiles and the residual of density are shown in Fig. 5.7 and 5.8, respectively. As the entropy wave is convected downstream by the mean flow, acoustic waves are generated when it passes through the nozzle. Fig. 5.9 and 5.10 present the instantaneous density and pressure distributions at different times, illustrating the acoustic response induced by the entropy perturbation. While $N = 600$ was used in [1] for the same DG-P^2 setup, the present scheme with the optimal dispersion relations is able to capture the same acoustic features using only $N = 480$ cells, and the generation and downstream propagation of the acoustic waves induced by the entropy perturbation are well resolved. This indicates that the use of the upwind-biased numerical flux in DG framework reduces the mesh resolution requirement, allowing the acoustic features to be resolved with fewer grid points compared with the standard upwind flux.

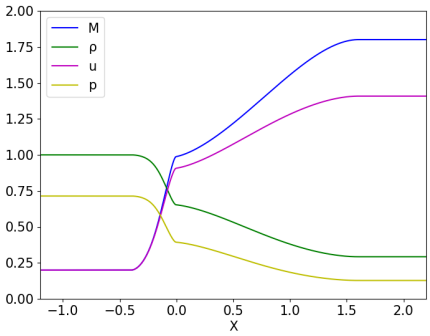

Fig. 5.7: Analytical mean flow of ρ, u, and p

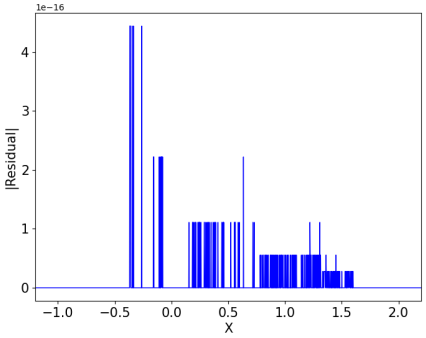

Fig. 5.8: Residual of ρ

Example 5.6. In this example, we consider the propagation of small amplitude acoustic waves superimposed on a mean flow in a convergent–divergent nozzle [30], which is shown in Fig. 5.11. The governing equations are identical to those used in **Example 5.5.** The duct area variation is prescribed

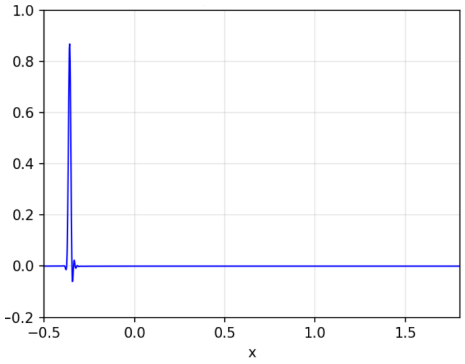

(a) $t = 4.2$

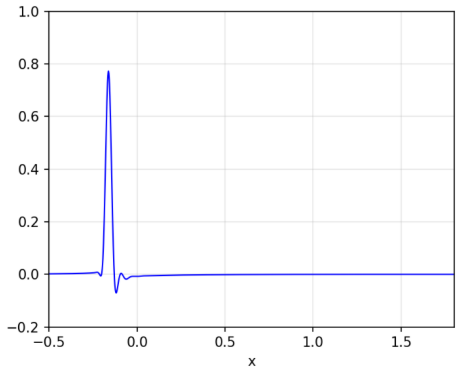

(b) $t = 4.9$

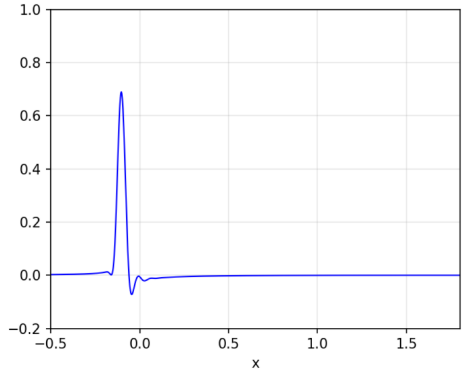

(c) $t = 5.0$

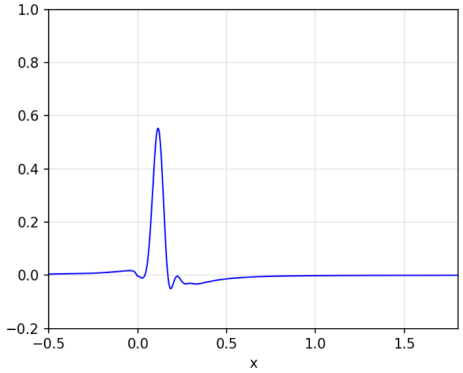

(d) $t = 5.3$

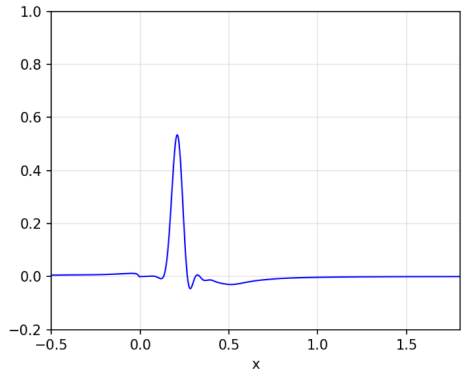

(e) $t = 5.4$

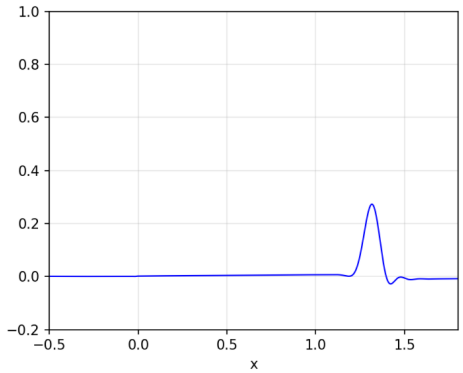

(f) $t = 6.3$

Fig. 5.9: The instantaneous density distributions inside the supersonic nozzle at six different times. The density perturbation are multiplied by 10^3.

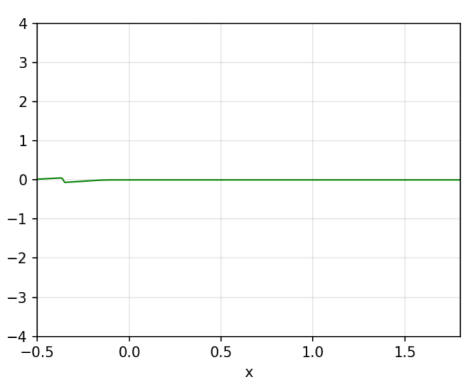

(a) $t = 4.2$

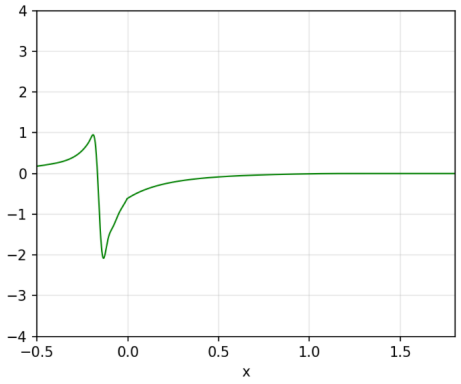

(b) $t = 4.9$

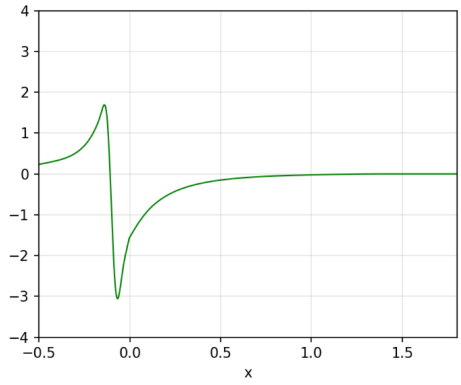

(c) $t = 5.0$

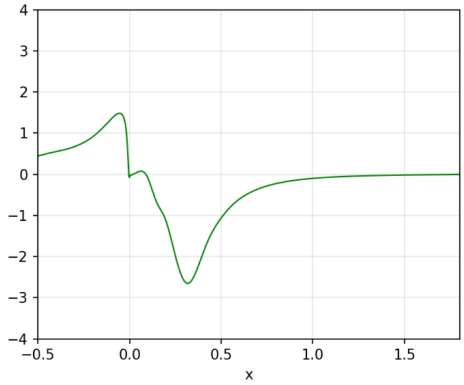

(d) $t = 5.3$

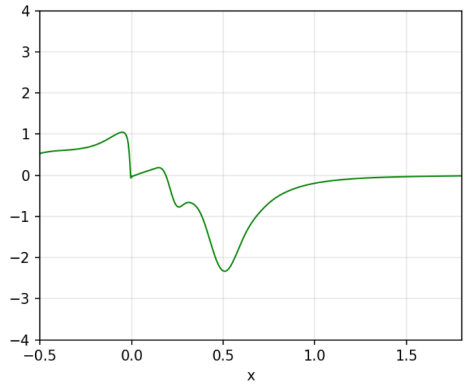

(e) $t = 5.4$

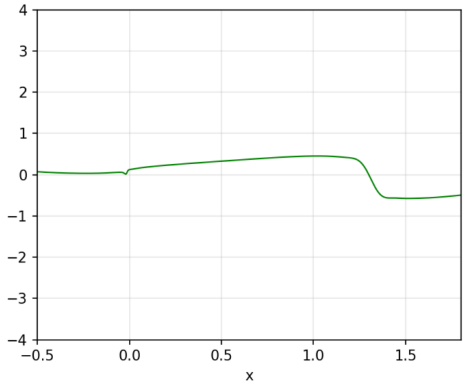

(f) $t = 6.3$

Fig. 5.10: The instantaneous pressure distributions inside the supersonic nozzle at six different time. The pressure perturbation are multiplied by 10^5.

as

$$A(x) = \begin{cases} \frac{134}{17} - 17\cos\left(\dfrac{\pi x}{100}\right), & -100 \le x \le 19, \\ 97.2 + 0.3x, & 19 \le x \le 80, \\ 1, & x \le -100. \end{cases}$$

The computational domain is chosen as $[-200, 80]$. The initial condition consists of a uniform mean flow with a small-amplitude acoustic perturbation,

$$\begin{bmatrix} u \\ p \\ \rho \end{bmatrix} = \frac{1}{M} \begin{bmatrix} M \\ 1 \\ 1 \end{bmatrix} + \varepsilon \begin{bmatrix} 1 \\ 1 \\ 1 \end{bmatrix} \sin\left(\omega\left(\frac{x}{1+M} - t\right)\right),$$

where $M = 0.5$ is the Mach number, $\varepsilon = 10^{-6}$ is the perturbation amplitude, and $\omega = 0.1\pi$ is the angular frequency. We use the method described in Sec. 4 and compute this problem with the DG-P^1 scheme and $N = 140$. To analyze the acoustic response, the pressure perturbation is observed at $x = 80$, and the computation is carried out until $t = 850$.

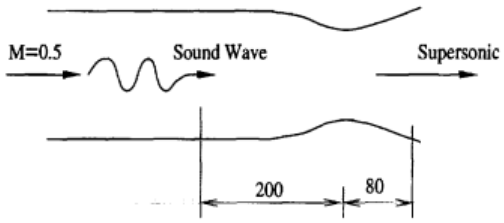

Fig. 5.11: Convergent–divergent nozzle for **Example 5.6.**

The analytical mean flow solution is shown in Fig. 5.12 while Fig. 5.13 presents the evolution of the pressure perturbation, demonstrating the propagation of acoustic waves through the convergent–divergent nozzle. Using the proposed scheme, the numerical results reproduce the acoustic features reported by Tam using a 7-point stencil DRP scheme for this problem [30], demonstrating that the DG method equipped with optimized dispersion properties provides an effective approach for resolving acoustic wave propagation problems.

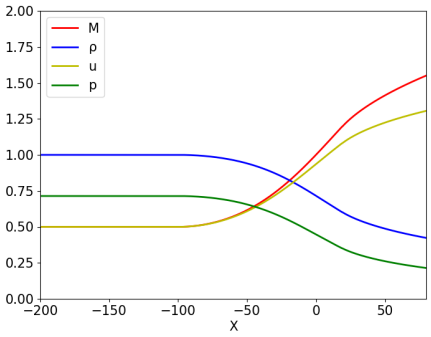

Fig. 5.12: Analytical mean flow of ρ, u, p and M

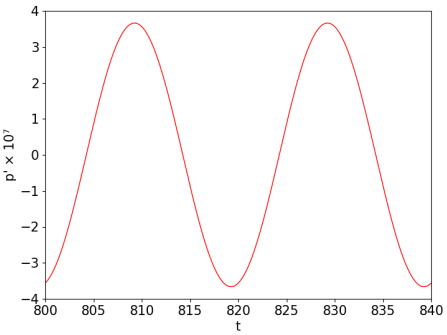

Fig. 5.13: Perturbation of pressure at the nozzle exit

6 Conclusion

In this paper, a dispersion and dissipation analysis of DG methods has been performed for linear hyperbolic problems. By analyzing the dispersion properties of the spatial discretization, optimized upwind-biased numerical flux parameters were derived for DG-P^q schemes with polynomial degrees from $q = 1$ to $q = 5$. The analysis shows that an appropriate choice of the θ values can substantially improve the dispersive properties of DG schemes while preserving stability. The resulting optimized flux provides a simple modification of the standard upwind flux and can be readily incorporated into existing DG frameworks.

Numerical experiments for scalar advection equations and linear hyperbolic systems confirm the theoretical findings, demonstrating consistent reductions in numerical errors when the optimized flux is employed. Additional tests involving geometric source terms, aliasing effects, and acoustic wave propagation in variable-area ducts and transonic nozzles further illustrate the robustness and effectiveness of the proposed approach in realistic wave propagation and computational aeroacoustics problems. These results indicate that optimal dispersion upwind-biased fluxes offer an efficient and practical strategy for improving the accuracy of DG methods for wave-dominated problems. Future work will focus on extensions to fully discrete DG methods, multidimensional and nonlinear problems.

Funding

F. Yan was partially supported by National Natural Science Foundation of China (No. 12501505) and Anhui Provincial Natural Science Foundation

(No. 2408085QA020). Y. Jiang was partially supported by the National Natural Science Foundation of China (No. 12271499). Z. Cheng was partially supported by the National Natural Science Foundation of China (Nos. 12201169, 32371555).

Data Availability

Data will be made available from the corresponding author upon reasonable request.

Declarations

Conflict of interest

The authors declare that there is no conflict of interest regarding the publication of this paper.

References

1. Z. Cheng, J. Fang, C.-W. Shu, and M. Zhang, Assessment of aeroacoustic resolution properties of DG schemes and comparison with DRP schemes, *Journal of Computational Physics*, 399:108960, 2019.

2. X. Meng, C.-W. Shu, and B. Wu, Optimal error estimates for discontinuous Galerkin methods based on upwind-biased fluxes for linear hyperbolic equations, *Mathematics of Computation*, 85(299):1225–1261, 2016.

3. D. J. Frean and J. K. Ryan, Superconvergence and the numerical flux: a study using the upwind-biased flux in discontinuous Galerkin methods, *Communications on Applied Mathematics and Computation*, 2(3):461–486, 2020.

4. H. Yang, F. Li, and J. Qiu, Dispersion and dissipation errors of two fully discrete discontinuous Galerkin methods, *Journal of Scientific Computing*, 55(3):552–574, 2013.

5. C. K. W. Tam and J. C. Webb, Dispersion-relation-preserving finite difference schemes for computational acoustics, *Journal of Computational Physics*, 107(2):262–281, 1993.

6. P. Sagaut, V. K. Suman, P. Sundaram, M. K. Rajpoo, Y. G. Bhumkar, S. Sengupta, A. Sengupta, and T. K. Sengupta, Global spectral analysis: review of numerical methods, *Computers & Fluids*, 261:105915, 2023.

7. T. K. Sengupta, P. Sagaut, A. Sengupta, and K. Saurabh, Global spectral analysis of three-time level integration schemes: Focusing phenomenon, *Computers & Fluids*, 157:182–195, 2017.

8. Y. Li and Y.-X. Ren, A scale-aware dispersion-relation-preserving finite difference scheme for computational aeroacoustics, *Physics of Fluids*, 35(3):036114, 2023.

9. C. K. W. Tam, J. C. Webb, and Z. Dong, A study of the short wave components in computational acoustics, *Journal of Computational Acoustics*, 1(1):1–30, 1993.

10. M. Zhuang and R. F. Chen, Optimized upwind dispersion-relation-preserving finite difference scheme for computational aeroacoustics, *AIAA Journal*, 36(11), 1998.

11. C. K. W. Tam, Computational aeroacoustics: issues and methods, *AIAA Journal*, 33(10), 1995.

12. B. Cockburn, S.-Y. Lin, and C.-W. Shu, TVB Runge-Kutta local projection discontinuous Galerkin finite element method for conservation laws III: one-dimensional systems, *Journal of Computational Physics*, 84(1):90–113, 1989.

13. B. Cockburn, S.-Y. Lin, and C.-W. Shu, The Runge-Kutta local projection discontinuous Galerkin finite element method for conservation laws IV: the multidimensional case, *Mathematics of Computation*, 54(190):545–581, 1990.

14. B. Cockburn and C.-W. Shu, The Runge-Kutta discontinuous Galerkin method for conservation laws V: multidimensional systems, *Journal of Computational Physics*, 141(2):199–224, 1998.

15. W. H. Reed and T. R. Hill, Triangular mesh methods for the neutron transport equation, Los Alamos Scientific Laboratory Technical Report, 1973.

16. B. Cockburn and C.-W. Shu, The Runge-Kutta local projection discontinuous Galerkin finite element method for scalar conservation laws, *ESAIM: Mathematical Modelling and Numerical Analysis*, 25(3):337–361, 1991.

17. M. Ainsworth, Dispersive and dissipative behaviour of high order discontinuous Galerkin finite element methods, *Journal of Computational Physics*, 198(1):106–130, 2004.

18. S. Sengupta, N. A. Sreejith, P. Mohanamuraly, G. Staffelbach, and L. Gicquel, Global spectral analysis of the Lax–Wendroff-central difference scheme applied to Convection–Diffusion equation, *Computers & Fluids*, 242:105508, 2022.

19. Q. Chen, Z. Sun, and Y. Xing, The Runge–Kutta discontinuous Galerkin method with compact stencils for hyperbolic conservation laws, *SIAM Journal on Scientific Computing*, 46(2):A1327–A1351, 2024.

20. C. Cheong and S. Lee, Grid-optimized dispersion-relation-preserving schemes on general geometries for computational aeroacoustics, *Journal of Computational Physics*, 174(1):248–276, 2001.

21. S. J. Sherwin, Dispersion analysis of the continuous and discontinuous Galerkin formulations, in *Discontinuous Galerkin Methods*, Springer, pp. 425–431, 2000.

22. F. Q. Hu, M. Y. Hussaini, and P. Rasetarinera, An analysis of the discontinuous Galerkin method for wave propagation problems, *Journal of Computational Physics*, 151(2):921–946, 1999.

23. L. Liu, X. Li, and F. Q. Hu, Nonuniform time-step Runge-Kutta discontinuous Galerkin method for computational aeroacoustics, *Journal of Computational Physics*, 229(19):6874–6897, 2010.

24. Y. Xu, D. Zhao, and Q. Zhang, Local error estimates for Runge-Kutta discontinuous Galerkin methods with upwind-biased numerical fluxes for a linear hyperbolic equation in one-dimension with discontinuous initial data, *Journal of Scientific Computing*, 91(1):11, 2022.

25. M. Liu, B. Wu, and X. Meng, Optimal error estimates of the discontinuous Galerkin method with upwind-biased fluxes for 2D linear variable coefficients hyperbolic equations, *Journal of Scientific Computing*, 83(1):9, 2020.

26. J. Li, D. Zhang, X. Meng, and B. Wu, Analysis of discontinuous Galerkin methods with upwind-biased fluxes for one dimensional linear hyperbolic equations with degenerate variable coefficients, *Journal of Scientific Computing*, 78(3):1305–1328, 2019.

27. M. Alhawwary and Z. J. Wang, Fourier analysis and evaluation of DG, FD and compact difference methods for conservation laws, *Journal of Computational Physics*, 373:835–862, 2018.

28. M. D. Dahl, Third computational aeroacoustics (CAA) workshop on benchmark problems, NASA Conference Publication 2000-209790, 2000.

29. M. D. Dahl, Fourth computational aeroacoustics (CAA) workshop on benchmark problems, NASA Conference Publication 2004-212954, 2004.

30. J. C. Hardin, J. R. Ristorcelli, and C. K. W. Tam, ICASE/LaRC workshop on benchmark problems in computational aeroacoustics (CAA), NASA Conference Publication 3300, 1995.

31. C. K. W. Tam and K. A. Kurbatskii, Multi-size-mesh multi-time-step dispersion-relation-preserving scheme for multiple-scales aeroacoustics problems, *International Journal of Computational Fluid Dynamics*, 17(2):119–132, 2003.

32. H. Yu, Z. Cheng, and Y. Jiang, Global spectral analysis of two fully discrete discontinuous Galerkin methods on unfitted meshes, *Journal of Scientific Computing*, 105(2):54, 2025.

33. S. Gottlieb and C.-W. Shu, Total variation diminishing Runge-Kutta schemes, *Mathematics of Computation*, 67(221):73–85, 1998.

34. B. Cockburn and C.-W. Shu, TVB Runge–Kutta local projection discontinuous Galerkin finite element method for conservation laws II: General framework, *Mathematics of Computation*, 52(186):411–435, 1989.